JOURNAL OF GEOPHYSICAL RESEARCH, VOL. 101, NO. C10, PAGES 25,647–25,659, NOVEMBER 15, 1996

A robust method for diagnosing regional shelf circulation from scattered density profiles

Jinyu Sheng and Keith R. Thompson

Department of Oceanography, Dalhousie University, Halifax, Nova Scotia, Canada

Abstract. We present a straightforward method for estimating surface circulation on an f plane from a set of irregularly spaced vertical density profiles. The first step is to express bottom density ρ_h as the sum of a mean $\tilde{\rho}_h$ for a given water depth h and an anomaly, $\rho'_h = \rho_h - \tilde{\rho}_h$. Sea level η can then be decomposed into a dynamic height $\tilde{\eta}$ relative to a deep reference level and a correction term, $\eta' = \eta - \tilde{\eta}$. The dynamic height is estimated using a generalization of the method of *Helland-Hansen* [1934] for diagnosing flow through a cross-shelf section under the assumption of zero bottom geostrophic flow. The correction η' satisfies a two-dimensional elliptic partial differential equation forced by the bottom density anomaly, wind stress and the open boundary conditions. Before calculating the density-driven component of η' we first test if the ρ'_h are statistically different from uncorrelated noise. If they are not, the correction associated with the bottom density anomaly is set to zero. Thus the method has a degree of robustness to errors in the density observations. If the ρ'_h have well-defined spatial structure the elliptic equation is solved for η' and sea level is equated to $\tilde{\eta} + \eta'$. Note that even if this last step is required the only gridding of the density data is two-dimensional. This makes the proposed method simpler to use than many of the existing diagnostic models which require a three-dimensional gridding of the observed density profiles. To test the method, we use it to diagnose the flow from an idealized density field overlying an isolated topographic feature. The predicted sea level and flow fields are then compared, and shown to be in good agreement, with results from the Princeton Ocean Model. The method is then used to diagnose the winter surface circulation on the Scotian Shelf from observed density profiles. The reliability of the diagnosed flow pattern is assessed by comparing it against all available near-surface current measurements. The differences between the observed and diagnosed currents are used to estimate the remotely forced circulation on the Scotian Shelf. It is shown that the main features of the circulation can be explained by gradients in the density field. Remote forcing is important near the coast and the shelf break. The effect of local wind is relatively weak.

1. Introduction

The diagnosis of shelf circulation from density observations has a history stretching back at least 60 years (see *Defant* [1961] for an historical review). The present generation of diagnostic models is quite sophisticated and can accommodate arbitrary bottom topography, turbulence closure schemes, and general boundary conditions [e.g., *Mellor et al.*, 1982; *Huthnance*, 1984; *Lynch et al.*, 1992; *deYoung et al.*, 1993]. Our interest in diagnostic modeling came from the need to map shelf circulation in near real time. We needed a method that was efficient and robust to errors in the density observations. A difficulty we anticipated in using the existing diagnostic models was the accurate gridding in three dimensions of the small number of irregularly spaced density profiles to be collected. High accuracy is required because the diagnosed flow is known to be sensitive to small errors in the density field over steep bottom topography [e.g., *Sarkisyan and Ivanov*, 1971; *Sarmiento and Bryan*, 1982; *Bogden et al.*, 1993; *Ezer and Mellor*, 1994].

In this paper we present a modification of the existing methods for diagnosing the surface circulation of a shelf sea. The horizontal extent of the study area is assumed small enough that the f plane approximation is valid. The first step is to split the bottom density $\rho_h(x, y)$ into two parts:

$$\rho_h = \tilde{\rho}_h + \rho'_h, \tag{1}$$

where $\tilde{\rho}_h$ is bottom density averaged along isobaths of depth h, and $\rho'_h(x, y)$ is the local deviation about this

Paper number 96JC01331.
0148-0227/96/96JC-01331$09.00

mean. This decomposition allows the sea level η, and hence the surface geostrophic flow, to be decomposed in a similar way:

$$\eta = \tilde{\eta} + \eta', \tag{2}$$

where $\tilde{\eta}$ is dynamic height relative to a deep reference level ($z = -H$) and η' is a correction term. The dynamic height $\tilde{\eta}$ is defined locally in the sense that it depends only on the vertical density profile and its extrapolation from $z = -h$ to $-H$ by $\tilde{\rho}_h$. The correction η' satisfies a two-dimensional elliptic partial differential equation forced by ρ'_h, wind stress and flows through the open boundaries of the model. It is relatively easy to calculate the barotropic component of η' forced by the wind and boundary flows. To calculate the density-driven component of η' we first examine the spatial distribution of the ρ'_h and test if they are statistically different from uncorrelated noise. If not, the correction due to the bottom density anomaly is set to zero and the density-driven component of sea level is approximated by $\tilde{\eta}$. Thus the method has a degree of robustness to errors in the density observations. If the ρ'_h have well-defined spatial structure the elliptic equation is solved for η' and sea level equated to $\tilde{\eta} + \eta'$. Note that even if this last step is required the only gridding of the density data is two-dimensional. The proposed method is therefore simpler to use than many of the existing diagnostic models which require three-dimensional gridding of the observed density profiles.

There are strong similarities between our approach and those of *Helland-Hansen* [1934] and *Csanady* [1979]. To illustrate, consider a density section running across the shelf with water depth increasing monotonically with distance from shore. To estimate currents normal to the section using the Helland-Hansen approach the bottom geostrophic velocity is assumed zero and the rest of the flow field is estimated by integrating the thermal wind equation. *Csanady* [1979] extended this approach to allow for slow variations in density along the shelf. Such density variations will generally drive bottom geostrophic flow and Csanady showed that the associated sea level correction satisfies a parabolic partial differential equation which governs the "downstream diffusion" of the effect of the bottom density anomalies. Our approach allows for density and bathymetric variations both along and across the shelf. In the present notation $\tilde{\eta}$ is a first guess for the baroclinic component of sea level based on the assumptions of constant bottom density along isobaths and zero bottom geostrophic flow. η' is a correction term resulting from the relaxation of these assumptions.

The method is described in section 2 and applied to an idealized problem in section 3. It is used in section 4 to estimate the winter surface circulation on the Scotian Shelf from all density profiles collected over the last 70 years. Differences between observed and diagnosed near-surface currents are used to assess the importance of density gradients and to estimate the remotely forced component of flow. Results are summarized in section 5.

2. The Method

Under the hydrostatic approximation, pressure at depth z is given by

$$p = g\rho_0\eta + g\int_z^0 \rho dz, \tag{3}$$

where η is isostatically-adjusted sea level and the rest of the notation is standard. Following *Csanady* [1979], the linearized horizontal momentum equation for steady shelf circulation is taken to be

$$f\vec{k} \times \vec{u} = -\frac{1}{\rho_o}\nabla p + \frac{\partial \vec{\tau}}{\partial z}, \tag{4}$$

where $\vec{k}$ is an upward pointing unit vector, $\vec{u}$ is the horizontal velocity, ∇ is the horizontal gradient operator, and $\vec{\tau}$ is a Reynolds stress vector. Substituting (3) into (4) gives the following expression for the horizontal flow at depth z:

$$\vec{u} = \frac{\vec{k}}{f} \times \left[g\nabla\eta + \frac{g}{\rho_o}\int_z^0 \nabla\rho dz - \frac{\partial \vec{\tau}}{\partial z} \right]. \tag{5}$$

Vertically integrating over the water depth gives the following expression for horizontal transport:

$$\vec{U} = \frac{\vec{k}}{f} \times [gh\nabla(\eta - \eta_s) + \nabla\Phi - \vec{\tau}_0 + \vec{\tau}_h], \tag{6}$$

where

$$\eta_s = -\frac{1}{\rho_o}\int_{-h}^0 \rho dz, \tag{7}$$

$$\Phi = \frac{g}{\rho_o}\int_{-h}^o z\rho dz, \tag{8}$$

and $\vec{\tau}_0$, $\vec{\tau}_h$ are surface and bottom stresses, respectively. η_s is dynamic height relative to the sea floor and $\rho_o\Phi$ is the potential energy of the water column.

Equating the horizontal divergence of $\vec{U}$ to zero gives the following equation for sea level:

$$g\nabla(\eta - \eta_s) \times \nabla h = \nabla \times (\vec{\tau}_h - \vec{\tau}_0). \tag{9}$$

To interpret this equation, first note that the bottom geostrophic velocity may be written

$$\vec{u}_{gh} = \frac{g}{f}\vec{k} \times \left[\nabla(\eta - \eta_s) - \frac{\rho_h}{\rho_0}\nabla h \right]. \tag{10}$$

The vertical velocity at the bottom due to geostrophic flow across depth contours is then

$$-\vec{u}_{gh} \cdot \nabla h = -\frac{g}{f}\vec{k} \cdot [\nabla(\eta - \eta_s) \times \nabla h] \tag{11}$$

which is proportional to the left-hand side of (9). The vertical velocities into and out of the surface and bottom Ekman layers are

$$w_{0,h} = \vec{k} \cdot \left[\nabla \times \frac{\vec{\tau}_{0,h}}{f} \right]. \tag{12}$$

Noting that $w_h - \vec{u}_{gh} \cdot \nabla h$ is the vertical velocity just above the bottom Ekman layer [*Pedlosky*, 1979], it follows that (9) is just a simple balance of vertical velocities just outside the top and bottom Ekman layers.

Bottom pressure is equal to $g\rho_o(\eta - \eta_s)$. Thus (9) is similar to the formulation of *Rattray* [1982], who argued that working with bottom pressure is preferable to the stream function because the Joint Effect of Baroclinicity and Bottom Relief (JEBAR) is attenuated.

Before describing how to calculate η for arbitrary bottom topography, reconsider the simpler situation of a cross-shelf section with depths increasing monotonically with distance from shore. Helland-Hansen's method is equivalent to extending isopycnals horizontally under the sea floor from their point of intersection with it and then using the conventional dynamic height method with a level of no motion set at the maximum depth of the section, $z = -H$ say. Thus according to Helland-Hansen's method

$$\eta = \eta_s - \frac{1}{\rho_0}\int_{-H}^{-h} \rho_h dz. \tag{13}$$

Similar expressions were derived by *Montgomery* [1941] and *Csanady* [1979].

Helland-Hansen's method cannot be applied to a region where bottom density varies along isobaths because ρ_h is not uniquely defined. Our extension of Helland-Hansen's method is based on the decomposition of bottom density into a component averaged along isobaths and an anomaly as in (1). To illustrate the idea, Figure 1 shows an idealized density section across a bank and two points, A and B, at the same depth. The bottom densities at A and B are different and equal to ρ_4 and ρ_3, respectively. Taking the mean bottom density around the bank to be $\tilde{\rho}_h = (\rho_3 + \rho_4)/2$ gives $(\rho_4 - \rho_3)/2$ and $(\rho_3 - \rho_4)/2$ for the density anomalies at A and B, respectively.

The next step is to express sea level as the sum of two components, $\eta = \tilde{\eta} + \eta'$, where

$$\tilde{\eta} = \eta_s - \frac{1}{\rho_0}\int_{-H}^{-h} \tilde{\rho}_h dz, \tag{14}$$

and η' is a correction term. The only difference between

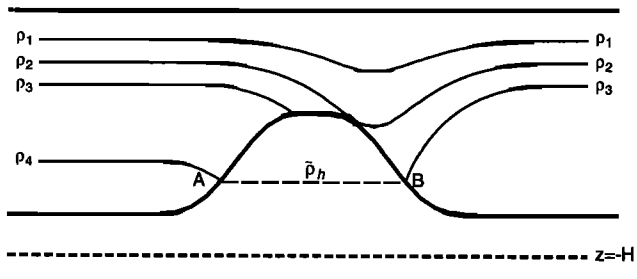

Figure 1. Schematic showing isopycnal surfaces intersecting the bottom at different depths. A are B are two points at the same water depth h. The mean bottom density $\tilde{\rho}_h$ around the bump at depth h is taken to be $(\rho_3 + \rho_4)/2$, giving density anomalies ρ'_h at A and B of $(\rho_4 - \rho_3)/2$ and $-(\rho_4 - \rho_3)/2$ respectively.

(13) and (14) is that ρ_h has been replaced by $\tilde{\rho}_h$.

From (6) the horizontal transport is given by

$$\vec{U} = \frac{\vec{k}}{f} \times \left[gh\nabla\eta' + \nabla\tilde{\Phi} - \vec{\tau}_0 + \vec{\tau}_h\right] \tag{15}$$

where

$$\tilde{\Phi} = \Phi + \frac{g}{\rho_o}\int_{-H}^{-h} z\tilde{\rho}_h dz, \tag{16}$$

and the bottom geostrophic velocity by

$$\vec{u}_{gh} = \frac{g}{f}\vec{k} \times \left[\nabla\eta' - \frac{\rho'_h}{\rho_0}\nabla h\right]. \tag{17}$$

Using the identity

$$\nabla(\eta - \tilde{\eta}) \times \nabla h = \nabla(\eta - \eta_s) \times \nabla h$$

in (9), or equivalently setting the horizontal divergence of (15) to zero, leads to the following equation for η':

$$g\nabla\eta' \times \nabla h = \nabla \times (\vec{\tau}_h - \vec{\tau}_0). \tag{18}$$

Following *Csanady* [1979] we parameterize bottom stress in terms of bottom geostrophic velocity:

$$\vec{\tau}_h = r\vec{u}_{gh}, \tag{19}$$

where r is a linear friction coefficient. (Linearization of the time-averaged quadratic stress law has been justified if the tides, or random fluctuations, dominate the mean. See for example, *Heaps* [1978], and *Wright and Thompson* [1983].)

Combining (19) and (17) it follows

$$\vec{k} \cdot \nabla \times \vec{\tau}_h = \frac{rg}{f}\left[\nabla^2\eta' - \nabla \cdot \left(\frac{\rho'_h}{\rho_0}\nabla h\right)\right] \tag{20}$$

and the governing equation for η' is

$$\nabla^2\eta' - \frac{f}{r}J(\eta', h) = \frac{1}{\rho_0}\nabla \cdot [\rho'_h \nabla h] + \frac{f^2}{rg}w_0 \tag{21}$$

where J denotes a Jacobian.

The open boundary conditions are fixed by specifying η'. The coastal boundary condition is no normal transport. Assuming water depth tends to zero as the coast is approached, it follows from (15) that the alongshore wind stress must be increasingly balanced by the alongshore component of bottom stress. Equation (19) then leads to an expression for the angled derivative of η' in terms of the alongshore component of wind stress and ρ'_h.

Examination of (21) and its boundary conditions reveals that η' is forced in three ways: by variations in bottom density along isobaths; by wind stress; and by flows through the open boundaries of the model. Thus we can write $\eta' = \eta'_d + \eta'_w + \eta'_b$ where subscript d, w, and b denote components forced by density, wind and the boundary flows, respectively. Calculation of the barotropic component $\eta'_w + \eta'_b$ is straightforward and

described in section 4. Calculation of the baroclinic component is summarized below:

1. Find the bottom density ρ_h for each density profile.
2. Estimate $\tilde{\rho}_h$ by fitting a function of water depth to ρ_h.
3. Use (14) to calculate $\tilde{\eta}$ for each density profile using $\tilde{\rho}_h$ as an extrapolating function of z.
4. Calculate the bottom density anomaly, $\rho'_h = \rho_h - \tilde{\rho}_h$, for each density profile.
5. Examine the spatial structure of ρ'_h. If it is indistinguishable from noise, set $\eta'_d = 0$ and $\eta = \tilde{\eta} + \eta'_w + \eta'_b$. Otherwise, solve (21) and set $\eta = \tilde{\eta} + \eta'_d + \eta'_w + \eta'_b$.

3. Circulation Over an Idealized Bank

In this section we compare predictions from the proposed method and the Princeton Ocean Model, a sophisticated primitive equation model with a sigma coordinate transformation in the vertical and an optional turbulence closure scheme. A recent description of the Princeton Ocean Model is given by *Ezer and Mellor* [1994].

Both models were used to diagnose the density-driven flow over an idealized bank (Figure 2a). The horizontal dimensions of the model domains are $L_x = 400$ km and $L_y = 200$ km and the grid spacing is uniform and equal to 10km for both models. Water depth is defined by

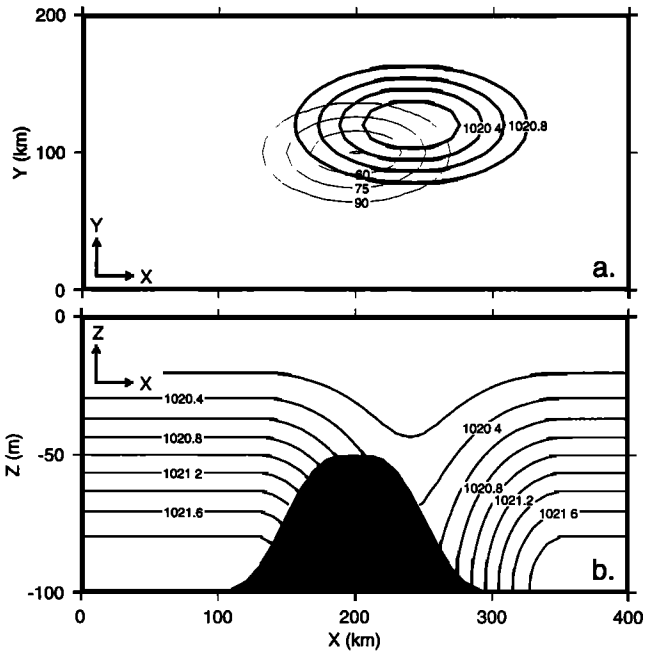

Figure 2. (a) Bathymetric contours (thin line, in m) of an idealized bank in a closed rectangular basin and density contours at 50 m (thick lines); (b) Bathymetry and isopycnals along $y = 100$ km.

$$h(x,y) = H - h_0 \exp(-40R^3), \tag{22}$$

where

$$R(x,y|x_0,y_0,l_x,l_y) = \sqrt{\frac{(x-x_0)^2}{l_x^2} + \frac{(y-y_0)^2}{l_y^2}} \tag{23}$$

with $x_0 = L_x/2$, $y_0 = L_y/2$, $l_x = L_x$ and $l_y = L_y$. H and h_0 are water depths in the far field and over the crest of the bank respectively. We take $H = 100$ m and $h_0 = 50$ m. The density field features a pool of lighter water offset slightly from the center of the bank (Figure 2b). It is defined by

$$\rho = \rho_0 + F(z)G(x,y)\Delta\rho \tag{24}$$

where

$$F(z) = \frac{1}{2}\left[1 - \cos(\frac{\pi z}{H})\right] \tag{25}$$

and

$$\begin{array}{lll} G(x,y) = & \frac{1}{2}[1-\cos(\pi R)] & R \le 1 \\ G(x,y) = & 1 & R > 1 \end{array} \tag{26}$$

with $R = R(x,y|0.6L_x, 0.6L_y, 0.3L_x, 0.3L_y)$. Note $F(0) = 0$ and so ρ_0 is the surface density. G equals unity in the far field and so $\Delta\rho$ is the surface-to-bottom density difference well away from the bank. We take $\rho_0 = 1020$ kg m^{-3} and $\Delta\rho = 2$ kg m^{-3}. For both models $f = 1.02 \times 10^{-4}$ s^{-1}. We also set $\vec{\tau}_0$ to zero and assume no transport through the model boundaries. Thus η'_w and η'_b are both zero in the proposed method.

Twenty four sigma levels are used in the Princeton Ocean Model. They are spaced linearly in the interior and logarithmically near the sea surface and sea floor. For simplicity, horizontal viscosity is set to zero and the turbulence closure scheme replaced by a constant vertical eddy viscosity of $\mu = 10^{-2}$ m^2 s^{-1}. Bottom stress is determined by matching velocities according to the logarithmic law of the wall. Specifically [*Blumberg and Mellor*, 1987]

$$\vec{\tau}_h = c_d|\vec{u}_h|\vec{u}_h, \tag{27}$$

with

$$c_d = \left[\frac{1}{\kappa}\ln(z_1/z_o)\right]^{-2}, \tag{28}$$

where $\kappa = 0.4$ is von Karman's constant, z_1 is the height of the first grid point off the bottom, and z_o is the roughness parameter which we take to be 1 cm [*Weatherly and Martin*, 1978].

For the proposed method we set $r = 5 \times 10^{-4}$ m s^{-1} and $\mu = 10^{-2}$ m^2 s^{-1}. The latter implies an Ekman depth of 14 m. Given the minimum water depth in the model domain is 50 m, the bottom Ekman layer will be fully developed. We therefore modified (19) to allow for a $\pi/4$ rotation of bottom stress relative to the bottom geostrophic current [e.g., *Pedlosky*, 1979]. This leads to a slightly more complicated version of (21) which we will not reproduce here.

Figure 3 is a scatterplot of bottom density against water depth. The line through the points is the estimated mean bottom density $\tilde{\rho}_h$ obtained by regressing ρ_h on a second-order polynomial in h. With $\tilde{\rho}_h$ thus defined, $\tilde{\eta}$ and ρ'_h were calculated using (14) and (1). As expected the low density pool causes a maximum in $\tilde{\eta}$ over the bank (Figure 4a). The bottom density anomaly has more spatial structure than $\tilde{\eta}$ (Figure 4b). Successive overrelaxation [e.g *Press et al.*, 1989] was used to calculate η'_d (Figure 4c). The variations in η'_d are about 20% those in $\tilde{\eta}$ and, for the present choice of parameters and density field, are similar to those of ρ'_h.

Contours of $\tilde{\eta} + \eta'_d$ are not as symmetric as those of density (Figure 5a). The anticyclonic surface geostrophic flow reaches a maximum speed of about 0.20 m s^{-1} (Figure 5b). The depth mean currents are roughly parallel to the surface currents (not shown) but somewhat weaker, everywhere less than 0.15 m s^{-1}.

We next ran the Princeton Ocean Model in diagnostic mode for 100 days, by which time the circulation was steady (Figure 6). We tried including the momentum advection terms but found they had little effect on the predicted flow fields. The steady-state results described below were obtained without these terms.

The sea level and current fields predicted by the two models are in good agreement (compare Figure 5 and Figure 6). For example, the maximum sea level from the Princeton Ocean Model is 5.9 cm, close to the maximum value of 6.1 cm obtained by the proposed method. There are however some slight differences. The most noticeable is that sea level and surface flow predicted by

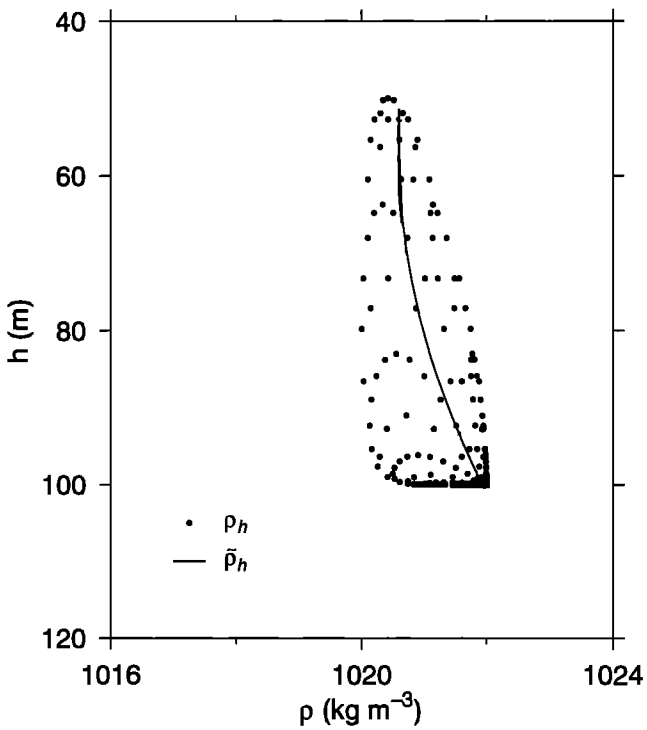

Figure 3. Scatterplot of bottom density ρ_h and water depth h for the idealized bathymetry and density field of Figure 2. The solid line is the mean bottom density $\tilde{\rho}_h$ as a function of h.

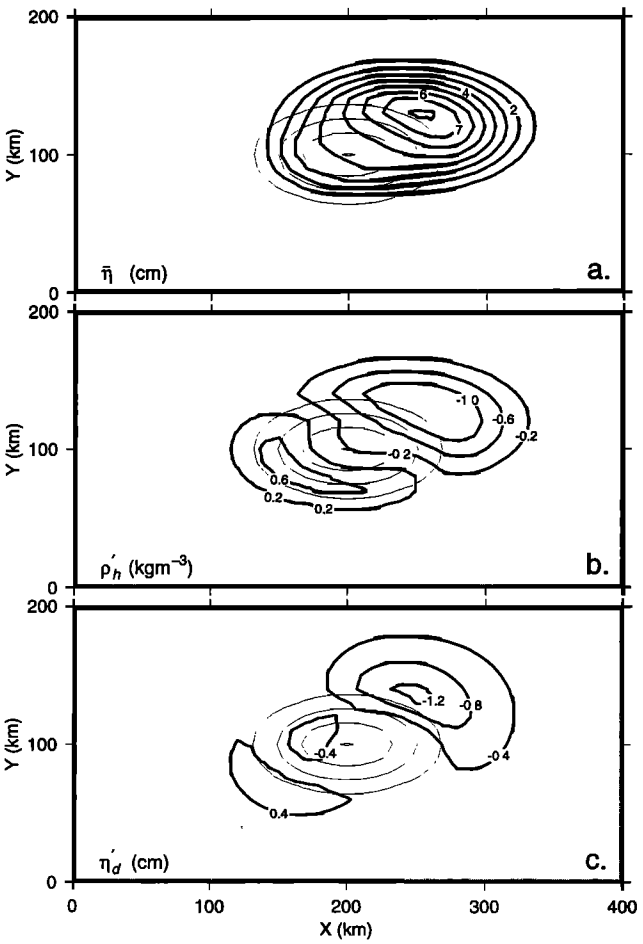

Figure 4. Fields of (a) sea level $\tilde{\eta}$; (b) bottom density anomaly ρ'_h; (c) sea level correction η'_d. All for the idealized bathymetry (thin lines) and density field of Figure 2.

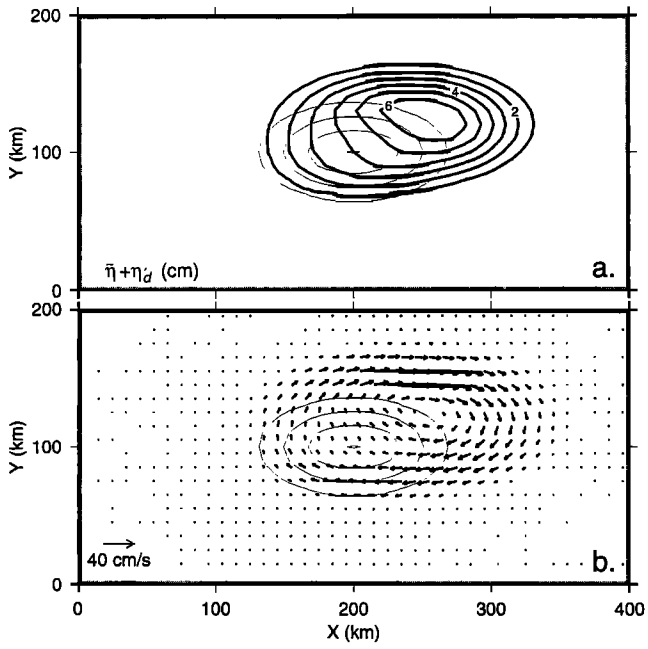

Figure 5. Fields of (a) sea level, $\tilde{\eta} + \eta'_d$; (b) associated surface geostrophic currents. Both for the idealized bathymetry (thin lines) and density field of Figure 2 calculated using the proposed method.

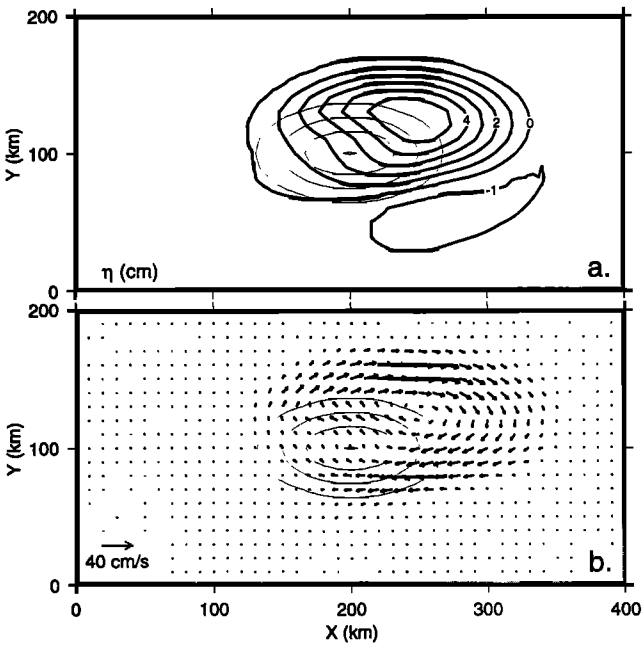

Figure 6. Fields of (a) sea level η; (b) associated surface geostrophic currents. Both for the idealized bathymetry (thin lines) and density field of Figure 2 calculated using the Princeton Ocean Model.

the Princeton Ocean Model are more variable over the bank. However on doubling the horizontal resolution of the Princeton Ocean Model, the sea level and flow fields became smoother and more similar to those calculated by the proposed method.

4. Circulation on the Scotian Shelf

To demonstrate the practical application of the method we now diagnose the winter circulation on the Scotian Shelf from observed density profiles (Figure 7). Earlier diagnostic calculations and direct current measurements suggest a southwestward drift along the shelf with intensified currents close to shore and along the shelf break. Freshwater runoff from the Gulf of St. Lawrence is believed to be important in driving the flow. (See *Smith and Schwing* [1991] for a review of the regional oceanography.)

4.1. Effect of Density Gradients ($\tilde{\eta}$ and η'_d)

All hydrographic data collected on the Scotian Shelf over the last 70 years between December and March were kindly provided to us by Ken Drinkwater of the Bedford Institute of Oceanography (Figure 7b). To minimize errors in estimating ρ_h we only used profiles with density measurements in the deepest 20% of the water column. Bottom density was estimated for each profile by linearly extrapolating the deeper observations to the sea floor. Figure 8 is a scatterplot of the extrapolated bottom densities against water depth. The solid line is an estimate of $\tilde{\rho}_h$ obtained by regressing the ρ_h on a second-order polynomial in h.

Dynamic height $\tilde{\eta}$ was calculated for each profile using the $\tilde{\rho}_h$ profile shown in Figure 8. (We took $H = 500$ m and $\rho_0 = 1025$ kg m^{-3}.) After eliminating less than 1% of the $\tilde{\eta}$ considered outliers, Barnes' algorithm [e.g., *Daley*, 1991] was used to interpolate the remaining $\tilde{\eta}$ onto a 1/10° grid. This algorithm is one of the more effective successive-correction methods used in mesoscale

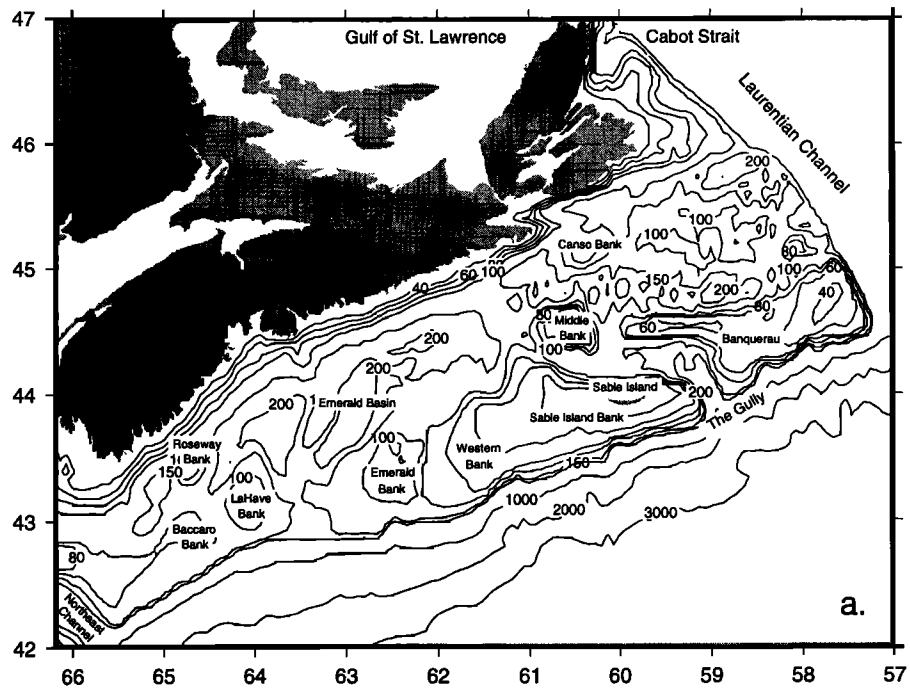

Figure 7. (a) Map showing the bathymetry (in meters) of the Scotian Shelf and some of its major features; (b) Positions at which vertical density profiles covering most of the water column have been made over the last 70 years between December and March.

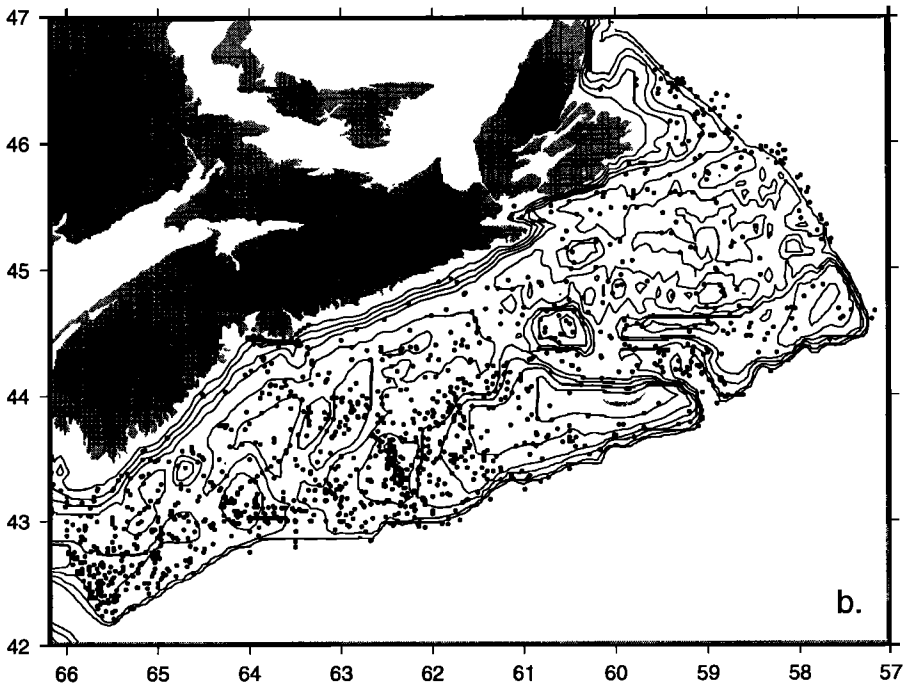

Figure 7. (continued)

analysis of radar and satellite data. As the number of iterations increases, the interpolated values approach the observations. The point at which to stop iterating is somewhat subjective: it depends in large part on the believability of the fitted fields, taking into account the spatial distribution of observations and their expected signal to noise ratio. The results presented in this paper are based on two iterations and an influence radius of about 40 km.

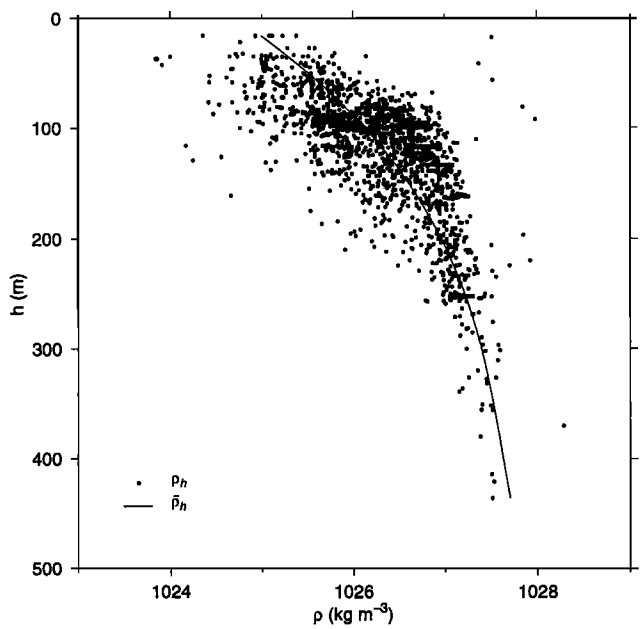

Figure 8. Bottom density ρ_h against water depth h for the winter density profiles from the Scotian Shelf. The solid line is the mean bottom density $\tilde{\rho}_h$ as a function of h.

The strongest gradients in $\tilde{\eta}$ are cross-shelf with $\tilde{\eta}$ dropping by about 10 cm from the coast to the shelf break (Figure 9a). The $\tilde{\eta}$ field has additional spatial structure. Note, for example, the sea level contours winding around Western Bank and passing through Emerald Basin. The surface geostrophic flow (Figure 9b) moves onto the Scotian Shelf from Cabot Strait as a broad current. It bifurcates south of Middle Bank with one branch turning toward the shelf break and the other turning northward and then westward as it approaches the coast. This coastal branch is reinforced by flow from the western flank of Western Bank before passing through Emerald Basin and then over LaHave Bank. Additional small-scale features are evident in-

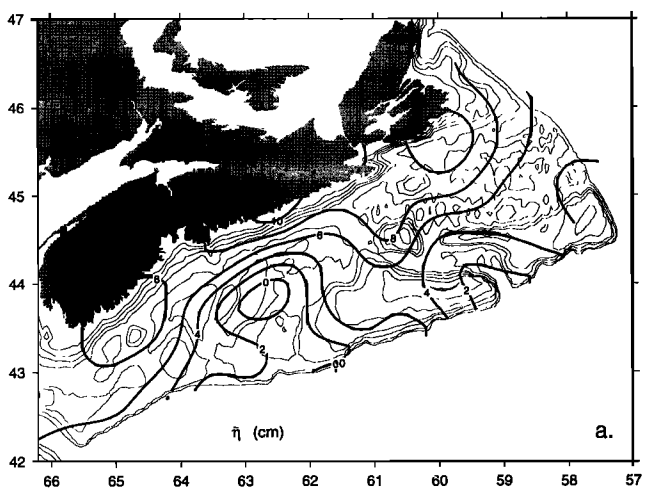

Figure 9. (a) Smoothed contours of dynamic height $\tilde{\eta}$. Smoothing was carried out using Barnes' algorithm as described in the text; (b) associated surface geostrophic currents.

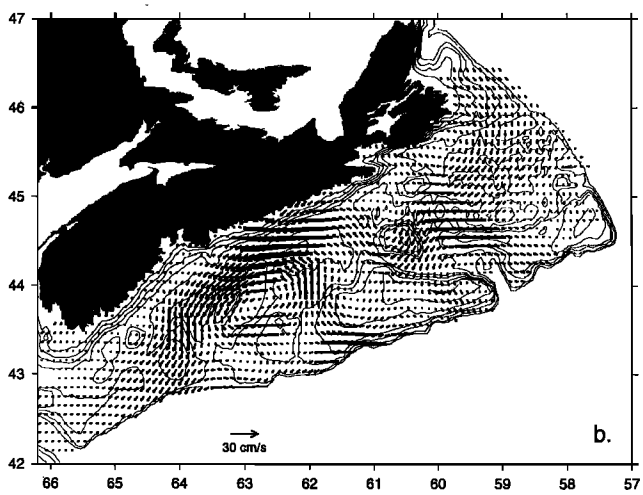

Figure 9. (continued)

cluding clockwise semi-gyres around Middle and Western Bank and a counterclockwise gyre over Emerald Basin.

To determine the spatial structure of ρ'_h, we estimated its spatial autocorrelation function. Each triangle in Figure 10 corresponds to a sample correlation calculated from about 40,000 pairs of ρ'_h with approximately the same separation distance. The correlation drops rapidly from unity to about 0.5 as the separation distance increases slightly from zero. This suggests a signal to noise variance ratio of $0.5^2/(1-0.5^2) = 1/3$. The shape of the autocorrelation function implies that the density anomalies have a characteristic wavelength of several hundred kilometers. Based on the shape and magnitude of the autocorrelation function we conclude that the ρ'_h cannot be treated as noise.

Contours of ρ'_h show that bottom density at a given depth is greater on Western and Emerald Bank than close to shore (Figure 11). This is perhaps the influ-

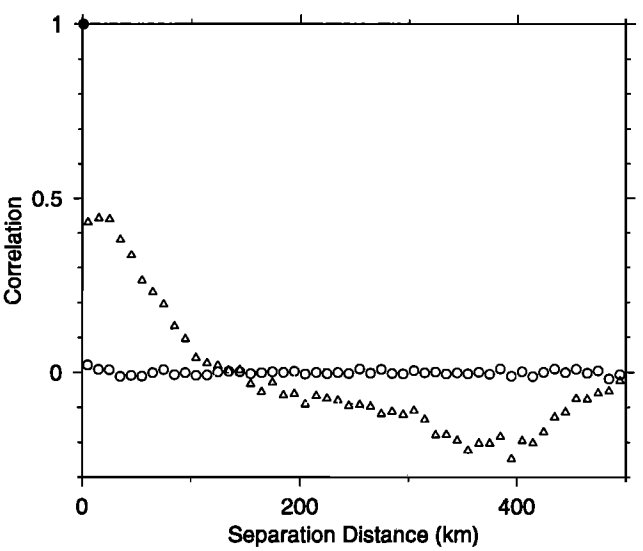

Figure 10. Correlation against separation distance of the bottom density anomalies (triangles) and their residuals (circles) after removal of the smoothed counterpart contoured in Figure 11.

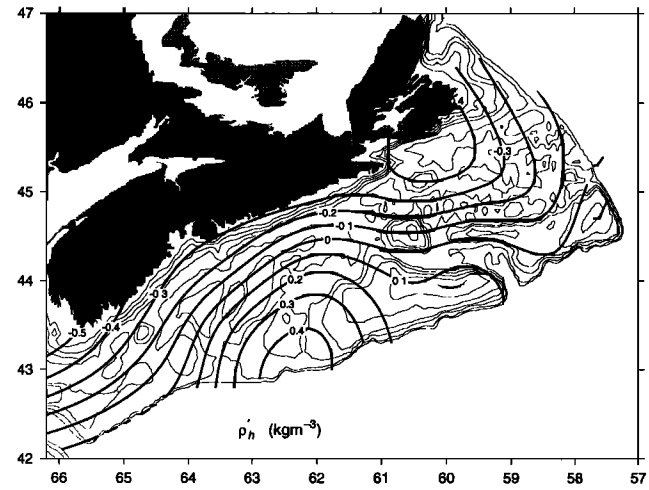

Figure 11. Smoothed contours of bottom density anomaly ρ'_h.

ence of freshwater runoff from the Gulf of St. Lawrence on the inner shelf and the intrusion of slightly heavier water from the Slope Water on the outer shelf. To confirm the smoothing applied to ρ'_h was adequate, we recalculated the autocorrelation function after removing from each ρ'_h its smoothed counterpart contoured in Figure 11. The discrepancies were statistically indistinguishable from spatially uncorrelated noise (Figure 10) implying that the important spatial structure in ρ'_h is captured by the field contoured in Figure 11.

To calculate η'_d, (21) was solved with wind stress and η'_d along the open boundary set to zero. The bathymetry was smoothed in the same way as ρ'_h for dynamical consistency. The $\tilde{\eta} + \eta'_d$ field is similar to that of $\tilde{\eta}$ (compare Figures 12a and 9a). The main difference is that $\tilde{\eta} + \eta'_d$ follows isobaths more closely than $\tilde{\eta}$, particularly over the inner shelf. This results in a stronger coastal jet, particularly on the western shelf (compare Figure 9b and 12b).

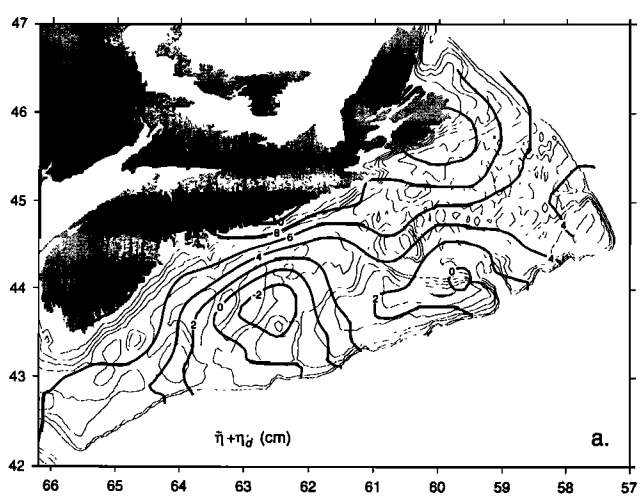

Figure 12. (a) Smoothed contours of $\tilde{\eta} + \eta'_d$; (b) associated surface geostrophic currents.

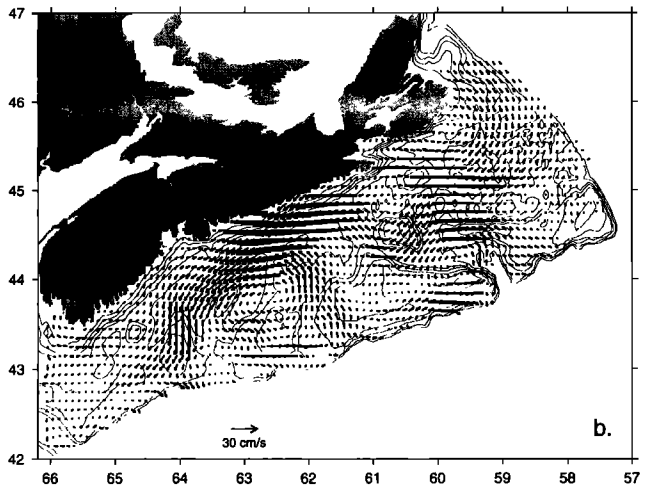

Figure 12. (continued)

4.2. Effect of Local Wind (η'_w)

The wind-driven component of sea level η'_w is the solution of (21) with ρ'_h set to zero. Surface Ekman pumping over eastern Canadian shelves is relatively weak in winter (O(10^{-6} m s^{-1}), see *Thompson and Hazen*, [1983]) and so w_0 was set to zero in (21). Wind stress was assumed spatially uniform. It was calculated from 40 years of wind observations from Sable Island. A radiation condition about a state of rest was applied along the open boundaries. After calculating η'_w, wind-driven currents $\vec{u}_w$ were calculated from (5) with ρ assumed constant and $\mu = 10^{-2}$ m^2 s^{-1}.

The maximum change in sea level driven by the mean winter wind stress ($\rho_o \vec{\tau}_0$ = (0.045, −0.016) Pa) is a 3 cm set-down along the coast of southwest Nova Scotia (Figure 13). The associated surface currents are weak, O(5 cm s^{-1}). They tend to follow the local coastline inshore of the 100 m isobath on the western shelf and agree with predictions from simple Ekman theory on the outer shelf.

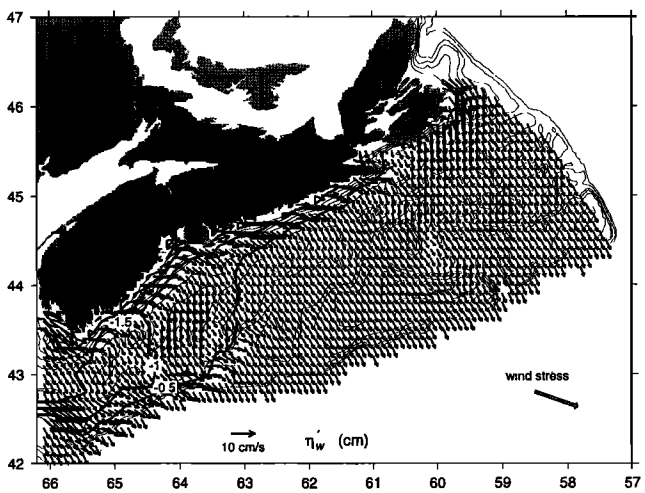

Figure 13. Surface currents and sea level η'_w driven by the mean winter wind stress at Sable Island.

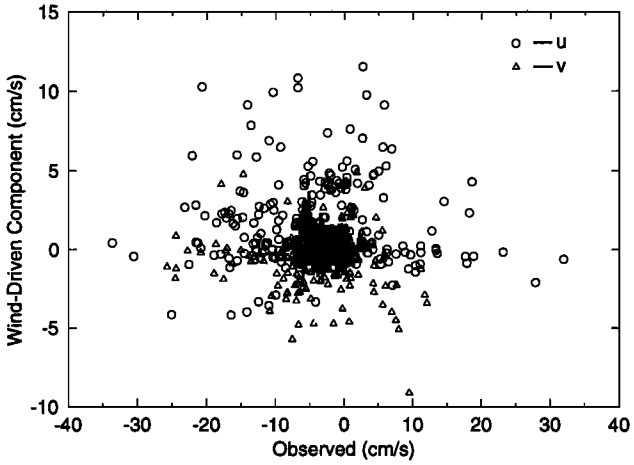

Figure 14. Scatterplot of wind-driven currents $\vec{u}_w$ and mean winter near-surface observations $\vec{u}_{\text{obs}}$. The northward and eastward components of flow are shown by triangles and circles respectively.

4.3. Model Validation

To assess the performance of the density and wind-driven sub-models we obtained from Doug Gregory of the Bedford Institute of Oceanography all the long (> 25 days) moored current meter time series recorded on the Scotian Shelf at depths less than 30 m during the period December through March. (See *Gregory and Smith* [1988] for a statistical summary of the data from 1966 to 1986). Mean wind-driven currents were then calculated for each current record using the wind from Sable Island averaged over the same period as the current record.

Figure 14 is a scatterplot of the observed and predicted currents. Clearly the wind-driven currents are much weaker than the observed currents. (The medians of the components of $\vec{u}_{\text{obs}}$ are (-4.8, -2.5) cm s^{-1} and their interquartile ranges are (10.3, 5.3) cm s^{-1}. The corresponding statistics for $\vec{u}_w$ are (0.8, -0.3) cm s^{-1} and (3.1, 1.6) cm s^{-1}.) To quantify the fit of the predictions to the observations, we introduce the sum of squared observations

$$J = \sum_{k=1}^{n} |\vec{u}_{\text{obs}}|_k^2 \tag{29}$$

and of the errors

$$J_w = \sum_{k=1}^{n} |\vec{u}_{\text{obs}} - \vec{u}_w|_k^2 \tag{30}$$

where $n = 46$ is the number of current means after averaging in the vertical if there was more than one meter on a mooring. We found $J_w/J = 1.16$. In other words the variance of the observations increases by 16% on removal of the wind effect. One reason is that the wind-driven currents are generally eastward, in the opposite direction to the observed currents. Thus subtracting $\vec{u}_d$ from $\vec{u}_{\text{obs}}$ increases the strength of the prevailing westward flow. Our conclusion based on J_w/J and Figure 14

is that the wind is not the primary cause of the winter circulation on the Scotian Shelf.

There is reasonable agreement between the wind-corrected observations $\vec{u}_{\text{obs}} - \vec{u}_w$ and the density-driven component of flow $\vec{u}_d$ (Figure 15). The density sub-model captures the relatively strong coastal jet and the onshore flow around the flank of Western Bank. However $\vec{u}_d$ fails to capture some important features evident in the $\vec{u}_{\text{obs}} - \vec{u}_w$. They include the strong shelf break current east of 60°W, the shear in the flow through the western boundary, and the fast flow in the trough between Emerald and LaHave Banks. We note however that the last discrepancy might be due to errors in the smoothed density field leading to a slight shift and attenuation of $\vec{u}_d$ in the vicinity of LaHave Bank (see Figure 12).

To quantify the fit of the density sub-model we introduce the following sum of squared errors:

$$J_{wd} = \sum_{k=1}^{n} |\vec{u}_{\text{obs}} - \vec{u}_w - \vec{u}_d|_k^2. \tag{31}$$

We found that $J_{wd}/J_w = 0.76$. Thus the variance of the wind-corrected observations is reduced by 24% on removal of the density-driven component of flow.

4.4. Effect of Boundary Inflows (η_b')

The remotely forced component of sea level η_b' is the solution of (21) with ρ_h', $\vec{\tau}_0$ set to zero and sea level specified along the open boundaries. The most important boundary for driving shelf circulation is the one "upstream" in the sense of coastal trapped wave propagation. It has long been recognized that outflow from the Gulf of St. Lawrence, and the southwestward flowing extension of the Labrador Current along the shelf break, exert an important influence on the overall circulation of the region [e.g., *Smith and Schwing*, 1991]. The upstream boundary condition was therefore specified in terms of two inflow jets: a coastal jet passing through the narrow cross-shelf section between Cape Breton Island and the Laurentian Channel (Figure 16a); an offshore jet entering the model domain at the shelf break (Figure 16b). The initial strengths of the jets were set by requiring the sea level drop across each jet to be 10 cm. Radiation conditions were applied along the other open boundaries.

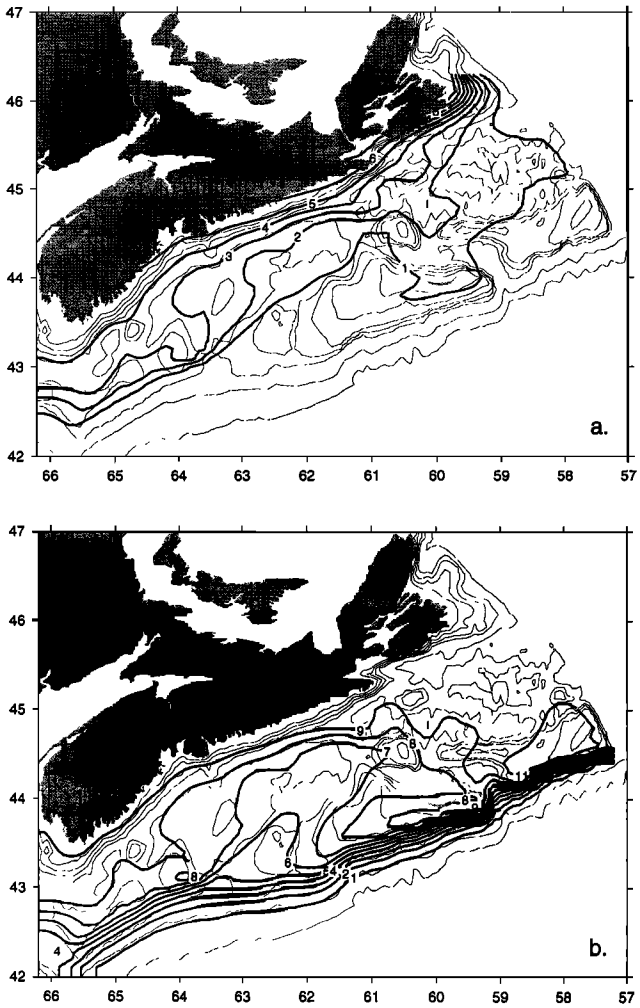

Figure 16. Sea level (in centimeters) forced by (a) 10 centimeter sea level drop over about 50 kilometers along that part of the open boundary running from Cape Breton to the Laurentian Channel; (b) a similar sea level drop at the shelf break.

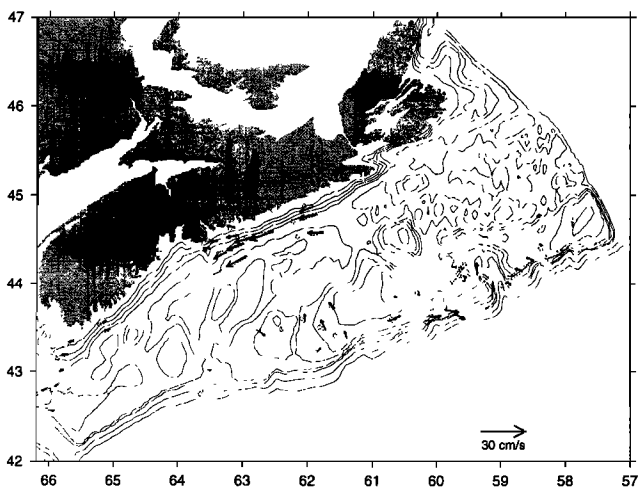

Figure 15. Comparison of mean winter near-surface observations with the wind effect removed ($\vec{u}_{\text{obs}} - \vec{u}_w$, dashed open arrows) and surface currents driven by local density gradients at the same locations ($\vec{u}_d$, solid arrows).

The circulation driven by the coastal and offshore jets are strongly controlled by bathymetry (Figure 16). The coastal jet can be clearly identified on the eastern part of the shelf (Figure 16a). It bifurcates on approaching Emerald Basin with one branch hugging the coast and the other heading southward and then westward along the shelf break. The offshore jet is strongly steered by the steep bathymetry at the shelf break. There is however some onshore flow through The Gully and the saddle between Western and Emerald Banks (Figure 16b).

To determine the relative strengths of the two jets we assume (see also *Sheng and Thompson* [1996]) the remotely forced circulation $\vec{u}_b$ can be linearly decomposed

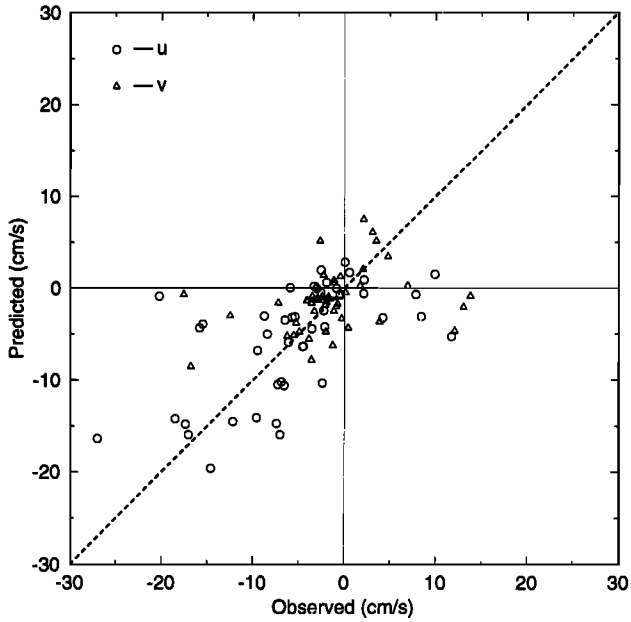

Figure 17. Scatterplot of observed and predicted near-surface currents on the Scotian Shelf. The observed are current observations with the wind effect removed ($\vec{u}_{\rm obs} - \vec{u}_w$). The predicted are due to local density gradients and boundary forcing ($\vec{u}_d + \vec{u}_b$). The northward and eastward components of flow are shown by triangles and circles, respectively.

as follows

$$\vec{u}_b = \alpha \vec{u}_i + \beta \vec{u}_o \tag{32}$$

where $\vec{u}_i$ and $\vec{u}_o$ are the flow fields associated with the inshore and offshore jets respectively, and α and β are unknown coefficients that determine their strengths. α and β were estimated by minimizing the sum of squared difference between the observed and predicted currents

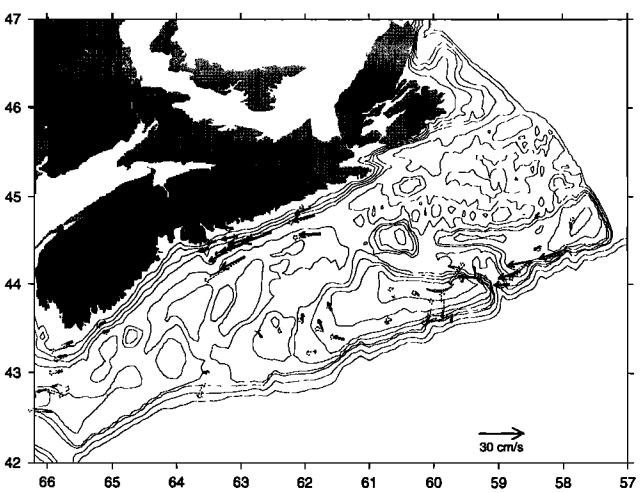

Figure 18. Comparison of observed (dashed open arrows) and predicted (solid arrows) near-surface currents on the Scotian Shelf. The observed are current observations with the wind effect removed ($\vec{u}_{\rm obs} - \vec{u}_w$). The predicted are due to local density gradients and boundary forcing ($\vec{u}_d + \vec{u}_b$).

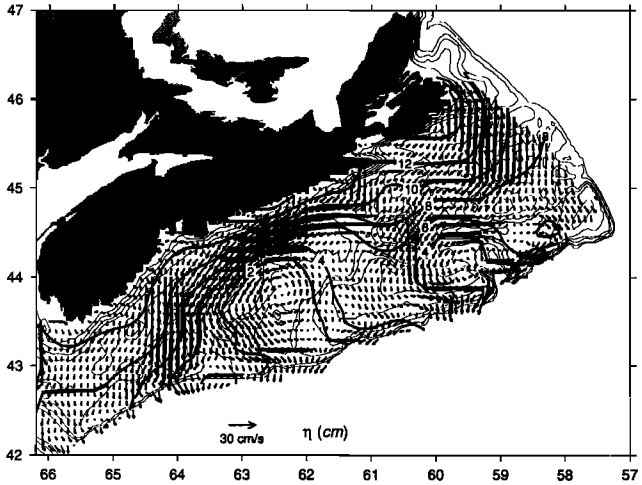

Figure 19. Predicted mean winter surface circulation on the Scotian Shelf ($\vec{u}_w + \vec{u}_d + \vec{u}_b$).

$$J_{\rm wdb}(\alpha, \beta) = \sum_{k=1}^{n} |\vec{u}_{\rm obs} - \vec{u}_w - \vec{u}_b - \vec{u}_d|_k^2. \tag{33}$$

At the minimum, $J_{\rm wdb}/J_w = 0.58$. Thus the variance of the wind-corrected observations is reduced by 42% on removal of the density and remotely forced components of flow. The optimal estimates of α and β are 0.22 and 0.27, respectively. This implies that the optimal sea level distribution along the northeast open boundary drops by 2.2 cm over the inner shelf and 2.7 cm across the shelf break.

Figure 17 is a scatterplot of components of $\vec{u}_b + \vec{u}_d$ against $\vec{u}_{\rm obs} - \vec{u}_w$. Overall, the agreement is quite reasonable. Comparison of Figure 18 and Figure 15 shows that allowance for remote forcing improves the predictions of the inshore jet, the onshore flow over Western Bank, and currents along the shelf break to the east of Sable Island.

The winter surface circulation on the Scotian Shelf predicted by $\vec{u}_d + \vec{u}_w + \vec{u}_b$ is shown in Figure 19. The broad, southwest flow over the eastern shelf splits into two branches on the central shelf: one flows northward and then westward as it approaches the coast; the other branch turns offshore and passes over Sable Island Bank. The coastal jet is deflected offshore by Emerald Basin after which it passes over LaHave Bank and the western flank of Emerald Bank.

5. Discussion

The proposed method for diagnosing shelf circulation is based on the decomposition of bottom density into a mean for a given depth $\tilde{\rho}_h$ and an anomaly ρ'_h. This allows sea level to be decomposed into a "local" dynamic height $\tilde{\eta}$ and a correction η'_d that satisfies an elliptic equation forced by ρ'_h. We recently used the method in an operational modeling exercise on Western Bank in which the flow was mapped in real time [*Griffin and Thompson*, 1996]. In this region, isopycnal

surfaces intersect the bottom approximately along isobaths ($\rho'_h \approx 0$), and so $gf^{-1}\vec{k} \times \nabla\tilde{\eta}$ is a good estimate of the surface geostrophic flow driven by density gradients. The fact that we did not have to project the limited number of density profiles onto a three-dimensional grid, a necessary step in the use of most conventional diagnostic models, greatly simplified the calculations and facilitated operational modeling.

One attractive feature of the proposed method is that it has some robustness to errors in the density observations. This is because one can test statistically if the bottom density anomalies have spatial structure before deciding whether or not to calculate η'_d. If the ρ'_h cannot be distinguished from noise then the simplest approach is to approximate η by $\tilde{\eta} + \eta'_w + \eta'_b$. This leads to a dynamically consistent estimate of the surface flow based on the assumption of zero bottom geostrophic flow. The corresponding transport stream function is given by $\Psi = \tilde{\Phi}/f$. If the ρ'_h have well-defined spatial structure a two-dimensional elliptic equation is solved for η'_d. Even in such circumstances the only gridding required is that of bottom density in two dimensions.

The definition of $\tilde{\rho}_h$, and hence $\tilde{\eta}$, are not unique. Our approach is to chose $\tilde{\rho}_h$ to minimize the mean square of the ρ'_h and thereby make $\tilde{\eta}$ a reasonable first guess for η. In general, $\tilde{\rho}_h$ and ρ'_h will change with the model domain. In particular, one may expect the variability in ρ'_h to increase with the size of the domain. This does not lead to inconsistencies in predicting the baroclinic flow. Circulation features generated by the density field within the domain of a large model will be forced in part by the boundary conditions of an embedded model.

To illustrate the practical application of the method we used it to estimate the winter surface circulation on the Scotian Shelf. Variations in the density field drive stronger currents than local wind or remote forcing in this region. The latter is limited mainly to the nearshore region and the shelf break. The density-driven component of flow in this region can be reasonably well approximated by surface geostrophic currents associated with $\tilde{\eta}$ which, in turn, can be estimated from individual density profiles. This opens the door to studies of interannual variability of the circulation in this region.

Acknowledgments. We thank Ken Drinkwater and Doug Gregory for providing the hydrographic and moored current meter data. Without their efforts this study would not have been possible. The authors are also grateful to Richard Greatbatch, Dan Wright, Brad deYoung and the reviewers for useful comments on the manuscript. This work was funded by OPEN (the Ocean Production Enhancement Network), one of the 15 networks of centers of excellence supported by the Government of Canada, and most recently by an award from IBM under their Environmental Research Program.

References

Blumberg, A., and G. L. Mellor, A description of a three-dimensional coastal ocean circulation model, in *Three-Dimensional Coastal Ocean Models, Coastal Estuarine Stud.* vol. 4, edited by N. Heaps, pp. 1-16, AGU, Washington, D.C, 1987.

Bogden, P. S., R. E. Davis, and R. Salmon, The North Atlantic circulation: Combining simplified dynamics with hydrographic data, *J. Mar. Res., 51*, 1-52, 1993.

Csanady, G. T., The pressure field along the western margin of the North Atlantic, *J. Geophys. Res., 84*, 4905-4915, 1979.

Daley, R., *Atmospheric Data Analysis*, 477 pp., Cambridge Univ. Press, New York, 1991.

Defant, A., *Physical Oceanography*, vol. 1, 729 pp., Pergamon, New York, 1961.

deYoung, B., R. J. Greatbatch, and K. B. Forward, A diagnostic coastal circulation model with application to Conception Bay, Newfoundland, *J. Phys. Oceanogr., 23*, 2617-2635, 1993.

Ezer, T., and G. Mellor, Diagnostic and prognostic calculations of the North Atlantic circulation and sea-level using a sigma coordinate ocean model, *J. Geophys. Res., 99*, 14,159-14,171, 1994.

Gregory, D. N., and P.C. Smith, Current statistics of the Scotian Shelf and Slope, *Can. Tech. Rep. Hydrogr. Ocean Sci., 106*, iv+197 pp., 1988.

Griffin, G. T., and K. R. Thompson, The adjoint method of data assimilation used operationally for shelf circulation, *J. Geophys. Res., 101*, 3457-3478, 1996.

Heaps, N. S., Linearized vertically-integrated equations for residual circulation in coastal seas, *Dtsch. Hydrogr. Z., 31*, 147-169, 1978.

Helland-Hansen, B., The Sognefjord section. Oceanographic observations in the northernmost part of the North Sea and the southern part of the Norwegian Sea, in *James Johnstone Memorial Vol.*, pp. 257-274, Lancashire Sea-Fish Lab., Univ. Press, Liverpool, 1934.

Huthnance, J. M., Slope currents and "JEBAR", *J. Phys. Oceanogr., 14*, 795-810, 1984.

Lynch, D. R., F.E. Werner, D. A. Greenberg, and J. W. Loder, Diagnostic model for baroclinic, wind-driven and tidal circulation in shallow seas, *Cont. Shelf Res., 12*, 37-64, 1992.

Mellor, G. L., C. R. Mechoso, and E. Keto, A diagnostic calculation of the general circulation of the Atlantic Ocean, *Deep Sea Res., 20*, 1171-1192, 1982.

Montgomery, R. B., Transport of the Florida Current off Havana, *J. Mar. Res., 4*, 198-219, 1941.

Pedlosky, J., *Geophysical Fluid Dynamics*, Springer-Verlag, New York, 1979.

Press W.H., B. P. Flannery, S. A. Teukolsky, and W. T. Vetterling, *Numerical Recipes*, Cambridge Univ. Press, New York, 1989.

Rattray, M., A simple exact treatment of the baroclinicity-bathymetry interaction in a frictional, iterative, diagnostic ocean model, *J. Phys. Oceanogr., 12*, 997-1003, 1982.

Sarkisyan, A. S., and V. F. Ivanov, The joint effect of baroclinicity and bottom relief as an important factor in the dynamics of ocean currents, *Izv. Acad. Sci. USSR, Atmos. Oceanic Phys., Engl. Trans., 7*, 173-188, 1971.

Sarmiento, J. L., and K. Bryan, An ocean transport model for the North Atlantic, *J. Geophys. Res., 87*, 394-408, 1982.

Sheng, J., and K. R. Thompson, Summer surface circulation on the Newfoundland Shelf and Grand Banks: The role of local density gradients and remote forcing, *Atmos. Ocean*, in press, 1996.

Smith, P. C., and F. B. Schwing, Mean circulation and variability on the eastern Canadian continental shelf, *Cont. Shelf Res., 11*, 977-1012, 1991.

Thompson, K. R., and M. G. Hazen, Interseasonal changes

of wind-stress and Ekman upwelling: North Atlantic, 1950-80, *Can. Tech. Rep. Fish. Aquat. Sci., 1214*, 1983.

Weatherly, G. L., and P. J. Martin, On the structure and dynamics of the oceanic bottom boundary layer, *J. Phys. Oceanogr., 8*, 557-570, 1978.

Wright, D. G., and K. R. Thompson, Time-averaged forms of the nonlinear stress law, *J. Phys. Oceanogr., 13*, 341-345, 1983.

J. Sheng and K. R. Thompson, Department of Oceanography, Dalhousie University, Halifax, Nova Scotia, Canada B3H 4J1

(Received February 1, 1995; revised February 9, 1996; accepted April 16, 1996.)